International Symposium
On Turbulence and Shear Flow
Phenomena (TSFP-9)
June 30 - July 3, 2015 *Melbourne, Australia*

LARGE-EDDY SIMULATION OF HIGHLY-DISTURBED TURBULENT FLOWS IN A V-SHAPED RIB-ROUGHENED DUCT

Xingjun Fang
Dept. of Mechanical Engineering
Univ. of Manitoba
Winnipeg, MB, R3T 5V6, Canada
fangx@cc.umanitoba.ca

Zixuan Yang
Dept. of Mechanical Engineering
Univ. of Manitoba
Winnipeg, MB, R3T 5V6, Canada
Zixuan.Yang@ad.umanitoba.ca

Bing-Chen Wang*
Dept. of Mechanical Engineering
Univ. of Manitoba
Winnipeg, MB, R3T 5V6, Canada
BingChen.Wang@ad.umanitoba.ca

Mark F. Tachie
Dept. of Mechanical Engineering
Univ. of Manitoba
Winnipeg, MB, R3T 5V6, Canada
Mark.Tachie@ad.umanitoba.ca

ABSTRACT

In this paper, highly-disturbed turbulent flows confined within a duct with equally spaced V-shaped ribs mounted on one wall are investigated using large-eddy simulation (LES). Two different inclined V-shaped (60° and 45°) rib cases are studied in comparison with the perpendicular (transverse) rib case. The results indicate that secondary flow appears as a pair of streamwise elongated vortices in all the cases, and its strength increases monotonically as the rib angle decreases. The effects of different shaped ribs on turbulence kinetic energy (TKE), TKE production rate and coherent structures are systematically investigated.

INTRODUCTION

Rib roughened surface in a low aspect ratio duct can enhance the momentum, mass and heat transfer, and is frequently employed in industrial applications, such as turbine blade cooling and heat exchangers. Based on various experimental evidences, Taslim *et al.* (1996) concluded that V-shaped ribs generate better heat transfer efficiency than transverse ribs in ducts of the same geometry. To optimize the design of rib-roughened walls for heat transfer enhancement, deeper understanding of the associated highly-disturbed turbulent flows is of crucial significance. Turbulent flow in a closed duct features interactions of turbulent boundary layers developed over all four walls (Gavrilakis, 1992). In addition, the strong disturbances generated by rib elements further induce large secondary flows which further dynamically interact with near-wall flow structures, making the turbulence field highly anisotropic in the cross-stream directions.

In literature, turbulent flow in a duct with transverse (90°) ribs has been numerically studied using LES, detached eddy simulation (DES) and Reynolds-average Navier-Stokes (RANS) approaches. Sewall *et al.* (2006) and Labbé (2013) demonstrated that LES can well predict the dominant physics of the flow, such as the first- and second-order turbulent statistics and heat transfer coefficient, in a duct with transverse ribs in comparison with the experimental results. Ooi *et al.* (2002) conducted simulations for turbulent flow and heat transfer in a square duct with one wall roughened by transverse ribs using different RANS turbulence models, and they attributed the poor accuracy of the resulted heat transfer coefficient to the failure of predicting correct secondary flow structures. Viswanathan & Tafti (2006) conducted DES and unsteady Reynolds-averaged Navier-Stokes (URANS) for a rotating duct with transverse ribs, and also concluded that URANS, due to its underlying defects, failed to capture major physics of the flow. As a useful numerical simulation tool, direction numerical simulations (DNS) can provide detailed information on the flow motion of all scales (from the largest integral scale to the finest Kolmogorov scales). However, at this stage, the computational cost of conducting DNS is still overly expensive for high Reynolds number flows. In view of this, LES is a more practical tool which can be performed at a considerably lower computational cost than DNS for transient numerical simulation of ribbed duct flows at moderate and high Reynolds numbers.

In comparison with the number of literatures on turbulent flow in a transverse-rib-roughened duct, fewer research works have been devoted to investigation of turbulent flow in a duct with inclined ribs. Bonhoff *et al.* (1999) studied turbulent flow over 45° inclined ribs using stereo particle image velocimetry (PIV). Gao & Sundén (2004*a*,*b*) investigated the turbulent flow in a high aspect ratio duct with V-shaped ribs pointing to the upstream and downstream directions using planar PIV. These previous investigations demonstrated the existence of strong secondary flows in the pattern of counter-rotating streamwise rotating vortices. Murata & Mochizuki (2001) also observed the existence of the secondary flow in the cross-stream directions in their LES study of heat and fluid flows confined within a stationary square duct with transverse and angled ribs. Tachie & Shah (2008) studied the effects of different inclined ribs on the turbulent flows subjected to a favorable pressure gradient. They indicated that the influences of inclined ribs on the distributions of mean velocity and Reynolds stresses can extend to the core region.

Notwithstanding the previous contributions mentioned above, the number of literatures on systematic study of highly-disturbed turbulent flows in a low aspect ratio duct is still limited. In view of this, we conduct a comparative study of V-shaped and perpendicular (transverse) rib-roughened duct flows using LES. We also thoroughly compare the numerical results with our newly acquired PIV experimental data (Fang *et al.*, 2015). The objective of this research is to investigate the physical mechanisms underlying the organized secondary flows and their effects on turbulence statistics and structures.

NUMERICAL ALGORITHM AND TEST CASES

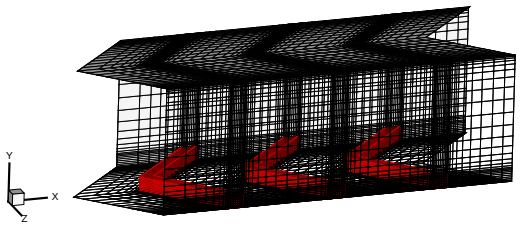

Figure 1. Computational domain, coordinates and grid system.

The geometry and body-fitted mesh for the test case are shown in Fig. 1. In the figure, the streamwise, vertical and spanwise coordinates are denoted using x, y and z axes, respectively. Periodically repeated V-shaped ribs are mounted on the bottom wall of a closed duct. Both cross-sections of the duct and ribs are square-shaped. The side length of the duct is denoted as 2δ and the rib height k is 10% of the duct height (i.e. $k = 0.2\delta$). The streamwise separation between two adjacent ribs (w) is 1.6δ, which gives the pitch-to-height ratio of $w/k = 8$. Three different angled (angle between ribs and the side walls) V-shaped ribs are studied, i.e. 90°, 60° and 45°. Here, the 90° inclined 'V-shaped' ribs correspond to the perpendicular (transverse) ribs. The computational domain consists of three ribs and its sizes are $4.8\delta \times 2\delta \times 2\delta$ in x, y and z directions, respectively. All the simulations are conducted based on $330 \times 176 \times 180$ body-fitted grids partially illustrated in Fig. 1. The mesh is refined near all solid walls, and the first grid is $2.5 \times 10^{-3}\delta$ off the wall. In particular, considering the complex flow physics in the near-rib region, 30 control volumes are used to cover both the rib width (x-direction) and height (y-direction). The time step is fixed to $2 \times 10^{-4}\delta/U_b$, where U_b represents the bulk mean velocity, and the resulted Courant number is approximately 0.2. The flow is driven by a mean streamwise pressure gradient Π (negatively valued), and the Reynolds number is fixed to $Re_b = U_b\delta/\nu = 5{,}000$.

To deal with the non-orthogonal geometry of V-shaped ribs, the governing equations are solved based on a generalized curvilinear coordinate (ξ_1, ξ_2, ξ_3), which take the following forms for an incompressible flow

$$\frac{1}{J}\frac{\partial\left(\beta_i^k \bar{u}_i\right)}{\partial \xi_k} = 0 \tag{1}$$

$$\begin{aligned}\frac{\partial \bar{u}_i}{\partial t} + \frac{1}{J}\frac{\partial}{\partial \xi_k}\left(\beta_j^k \bar{u}_i \bar{u}_j\right) = -\frac{1}{J\rho}\frac{\partial\left(\beta_i^k \bar{p}\right)}{\partial \xi_k} - \Pi\delta_{1i} \\ + \frac{\nu}{J}\frac{\partial}{\partial \xi_p}\left(\frac{1}{J}\beta_j^p \beta_j^q \frac{\partial \bar{u}_i}{\partial \xi_q}\right) - \frac{1}{J}\frac{\partial\left(\beta_j^k \tau_{ij}\right)}{\partial \xi_k}\end{aligned} \tag{2}$$

where $\bar{u}_i$ ($i = 1, 2$ and 3) (corresponding to $\bar{u}$, $\bar{v}$ and $\bar{w}$, respectively) are the resolved velocity components, and ρ, $\bar{p}$, ν, Π and τ_{ij} represent the density, effective pressure, kinematic viscosity, imposed constant streamwise mean pressure gradient and subgrid-scale (SGS) stresses, respectively. In the above equations, δ_{ij} represents the Kronecker delta, and β_j^i and J denote the cofactor and determinant of tensor $\partial x_i/\partial \xi_j$, respectively.

A finite volume method (FVM) based on a body-fitted collocated grid is used for the discretization of the above governing equations. A second-order central difference scheme is used for the spatial discretization and the second-order Rung-Kutta method is utilized for the time integration. As such, a second-order accuracy is achieved in both space and time. For each sub-step of the Rung-Kutta time marching scheme, a fractional-step method (Kim & Moin, 1985) is used and a pressure correction equation is solved by Parallel Extensible Toolkit for Scientific Computations (PETSc) library (Balay *et al.*,1997, 2014a,b) using an algebraic multigrid method. The momentum interpolation approach proposed by Rhie & Chow (1985) is implemented to establish the relation between the cell-face mass flux and the adjacent pressure difference, so that the 'checkerboard' pressure field is avoided. The dynamic Smagorinsky model (DSM) of Lilly (1992) is employed for modeling the SGS stress tensor τ_{ij}. Since no homogeneous direction exists in the current research, the model coefficient is spatially filtered to remove spurious fluctuations and then clipped to be positive to ensure the stability of the calculations.

The flow is assumed to be statistically stationary and spatially fully-developed. As such, periodic boundary conditions can be imposed at the inlet and outlet boundaries of the square duct. No-slip boundary conditions are applied to all solid walls.

In this paper, the resolved instantaneous velocity $\bar{u}$ is decomposed as $\bar{u} = \langle\bar{u}\rangle + \bar{u}''$, where the angular brackets $\langle\cdot\rangle$ denote the time-averaging over approximately 50 flow-through time (i.e, $240\delta/U_b$). To facilitate the comparisons between different rib cases, the origin of x axis is set at the leeward face of the first rib in the mid x-y plane (located at $z = 0$) for all the cases. In this paper, the 'experiment' refers to the PIV experiments conducted for the same cases by the same authors (Fang *et al.*, 2015). In the legends of plotted figures, notation V_{45} is used to indicate the 45° rib case, and so as V_{90} and V_{60}.

RESULTS AND DISCUSSIONS

To validate the numerical results in this paper, Fig. 2 compares the vertical profiles of $\langle\bar{u}\rangle$ and $\langle\bar{v}\rangle$ against the experimental data (Fang *et al.*, 2015) in the central plane (located at $z/\delta = 0$). Note that the 2-D bulk mean velocities in the central plane (U_{bc}) from the simulations and experiments are used to non-dimensionalize the corresponding velocities, since 3-D bulk mean velocity (U_b) is unavailable from the planar PIV measurement. According to the LES results, the ratios of U_{bc} to U_b for the 90°, 60° and 45° rib cases are 1.08, 1.11 and 1.18, respectively. As seen in the figures, the vertical profiles of mean streamwise velocity $\langle\bar{u}\rangle/U_{bc}$ acquired from LES are in good agreement with the experimental results; however, the magnitude of the mean vertical velocity $\langle\bar{v}\rangle/U_{bc}$ is overpredicted by LES for the V-shaped rib cases. From Fig. 2(a), it is clear there is a recirculation region (featuring a negatively valued streamwise velocity $\langle\bar{u}\rangle$) in the leeward region of the rib (under

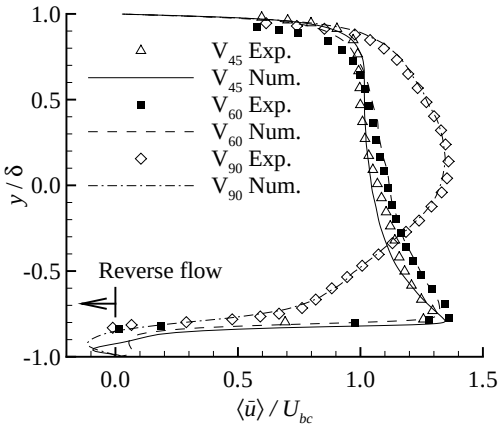

(a) Profiles of $\langle \bar{u} \rangle$

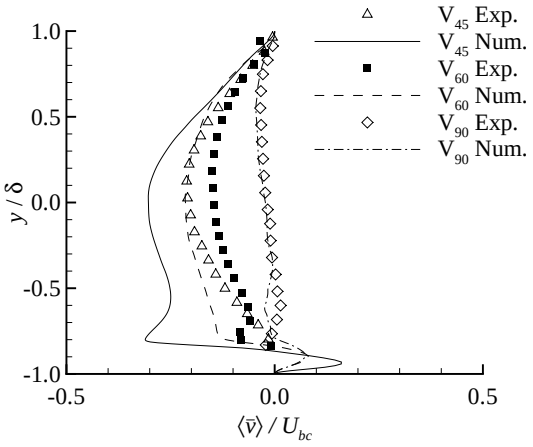

(b) Profiles of $\langle \bar{v} \rangle$

Figure 2. Comparisons of the vertical profiles of $\langle \bar{u} \rangle$ and $\langle \bar{v} \rangle$ at point $(x/\delta, z/\delta) = (0.8, 0.0)$ against PIV measurement data for different rib cases. For clarity, only 30% of the measured data are plotted.

the rib height). As the flow passes over the rib crest (at $y/\delta = -0.8$), a boundary layer briefly develops and soon separates from the rib, forming a strong shear layer around the rib crest. From Fig. 2(b), negatively valued $\langle \bar{v} \rangle$ can be observed above the rib height in the central plane for all the cases. In addition, the magnitude of $\langle \bar{v} \rangle$ increases monotonically as the rib angle decreases. This indicates the existence of strong cross-stream flows in V-shaped rib cases. Due to the downwash by negatively valued $\langle \bar{v} \rangle$, the peak value of $\langle \bar{u} \rangle$ is relocated to a vertical position that is very close to the rib crest in V-shaped rib cases.

To further study the cross-stream flows, Fig. 3 illustrates the contours of $\langle \bar{u} \rangle$ superimposed with in-plane streamlines in a cross-stream (y-z) plane for two different rib cases. It is evident from the figures that secondary flow appears in the pattern of streamwise elongated counter-rotating vortices pairs. Furthermore, in the V-shaped rib cases, because of the much large magnitude of $\langle \bar{v} \rangle$ (see, Fig. 2(b)), the strength of secondary flow is much stronger than that in the perpendicular rib case. These observations are consistent with PIV experiment of Fang *et al.* (2015).

Fig. 4 compares the vertical profiles of resolved

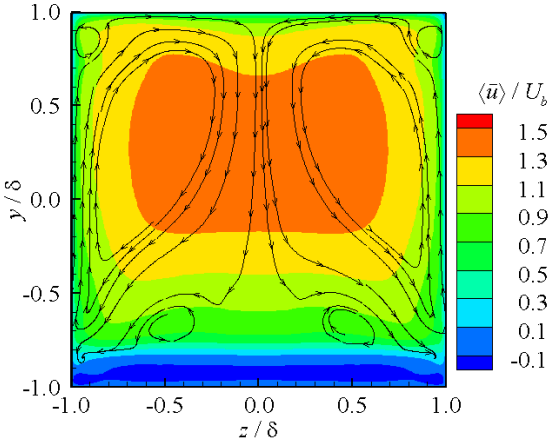

(a) 90° rib case

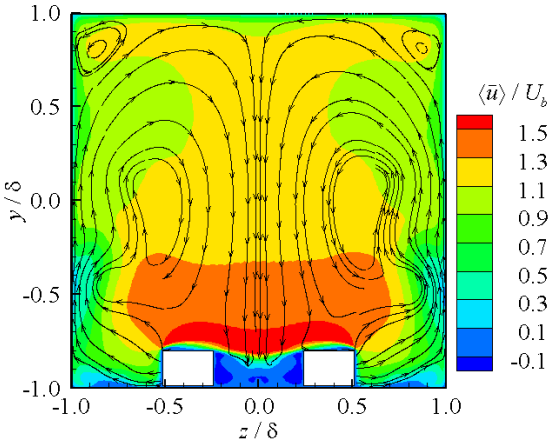

(b) 45° rib case

Figure 3. Contours of $\langle \bar{u} \rangle$ superimposed with in-plane streamlines in the y-z plane at $x/\delta = 0.2$ for different rib cases.

Reynolds stresses against the PIV measured data (Fang *et al.*, 2015). From Fig. 4, it is interesting to observe that for the V-shaped rib cases, the turbulence level (as indicated by the magnitudes of $\langle \bar{u}''\bar{u}'' \rangle$ and $\langle \bar{u}''\bar{v}'' \rangle$) below the rib height ($y/\delta < -0.8$) is significantly higher than that above the rib height ($y/\delta \geq -0.8$), which trend is consistent with the experimental results. To study the spatial distribution of turbulent intensity in the cross-stream directions, Fig. 5 compares the contours of resolved TKE (K) in the same y-z plane (located at $x/\delta = 0.2$) for the 90° and 45° rib cases. The 60° rib case exhibits a qualitatively similar pattern as the 45° rib case, and thus, it is not shown here to keep the discussion concise. It is observed in Fig. 5(a) that maximal TKE is mainly confined near the central region immediately above the crest of perpendicular ribs. In contrast, the region of high TKE level near the top of V-shaped ribs is very narrow in y direction. This is because that the strong vortex shedding events on top of the ribs are downwashed by the mean flow near the central region. In comparison with the perpendicular rib case, two spots with high levels of turbulent intensities are observed in the lower half duct near the two side walls. These observations indicate that the strong secondary flows in the V-shaped rib cases significantly alter the cross-stream distribution of the resolve TKE.

To further understand the resolved TKE distribution in

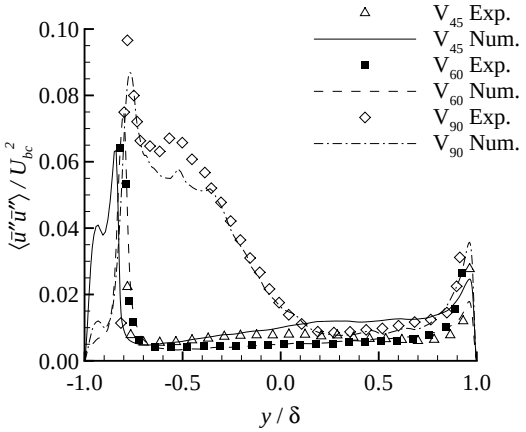

(a) Profiles of $\langle \bar{u}''\bar{u}'' \rangle$

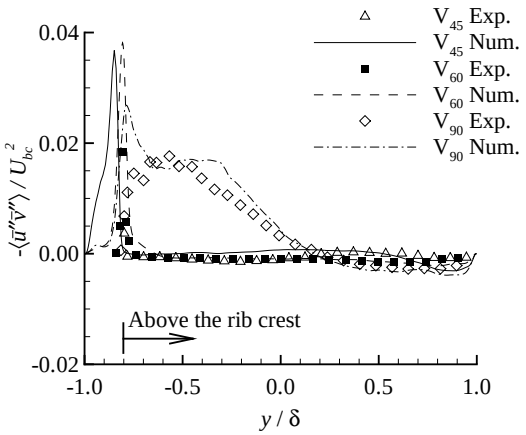

(b) Profiles of $-\langle \bar{u}''\bar{v}'' \rangle$

Figure 4. Comparisons of the vertical profiles of resolved Reynolds stresses at point $(x/\delta, z/\delta) = (0.2, 0.0)$ against PIV measurement data for different rib cases.

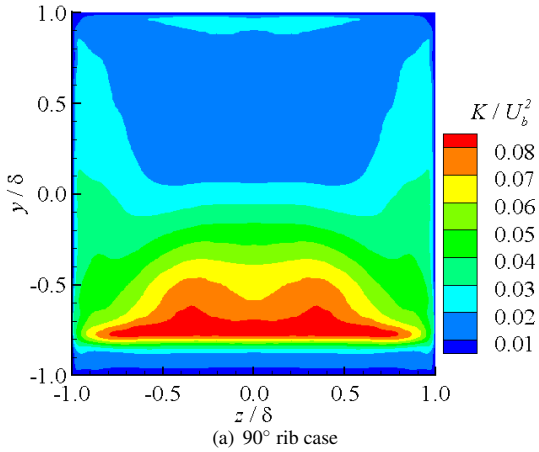

(a) 90° rib case

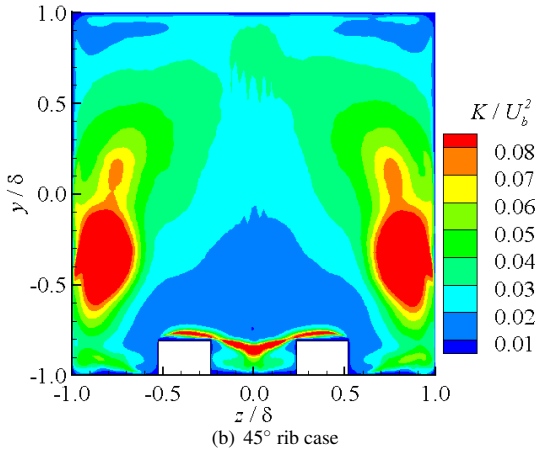

(b) 45° rib case

Figure 5. Contours of resolved TKE in the y-z plane at $x/\delta = 0.2$ for different rib cases.

the highly-disturbed mean flows of the studied cases, the resolved production term (P_{ij}) for $\langle \bar{u}_i'' \bar{u}_j'' \rangle$ can be investigated, which is defined as

$$P_{ij} = -\left\langle \bar{u}_i'' \bar{u}_k'' \right\rangle \frac{\partial \left\langle \bar{u}_j \right\rangle}{\partial x_k} - \left\langle \bar{u}_j'' \bar{u}_k'' \right\rangle \frac{\partial \left\langle \bar{u}_i \right\rangle}{\partial x_k} \tag{3}$$

Fig. 6 plots the contours of resolved production rate (P_{ii}) for TKE in a y-z plane for two different rib cases. From Fig. 6(a), the highest production of TKE is primarily concentrated near the vicinity of the perpendicular rib. In contrast, as seen in Figs. 6(b) for the 45° rib case, the region with a high TKE production rate near the rib crest is much reduced in y direction, and areas with intense TKE production are also observed in the lower half duct near the two side walls. The distribution pattern of the TKE production rate observed in this figure well explains the planar distribution of TKE shown previously in Fig. 5.

Fig. 7 compares the vertical profiles of resolved production terms P_{11}, P_{22}, P_{33} and P_{ii} for two different rib cases. All these quantities shown in the figures have been non-dimensionalized using U_b^3/δ. It is interesting to observe from Fig. 7(a) that compared with the smooth top wall, the perpendicular ribs induce much higher production rate of TKE in the bottom half $(y/\delta < 0.0)$ of the duct, and furthermore, most of the augmentation is contributed by $\langle \bar{u}_1'' \bar{u}_1'' \rangle$ component. These is because that the strong shear layer and vortices triggered by the top surfaces of the perpendicular ribs enhances the magnitude of $-\langle \bar{u}_1'' \bar{u}_2'' \rangle$ in the lower half duct (see, Fig. 4(c)), which further leads to augmentation in the production of $\langle \bar{u}_1'' \bar{u}_1'' \rangle$ through its resolved production term $-\langle \bar{u}_1'' \bar{u}_2'' \rangle \partial \langle \bar{u}_1 \rangle / \partial x_2$. As shown in the figure, the effects of ribs on the production of $\langle \bar{u}_3'' \bar{u}_3'' \rangle$ is almost negligible throughout the entire duct. However, in the region below the rib height, considerable production rate for $\langle \bar{u}_2'' \bar{u}_2'' \rangle$ is observed, which is primarily contributed by $-\langle \bar{u}_1'' \bar{u}_2'' \rangle \partial \langle \bar{u}_2 \rangle / \partial x_1$ (see, Eq. (3)). In comparison with the perpendicular rib case, as seen in Fig. 7(b), the enhancement of TKE production in V-shaped rib cases is mainly around the rib height, and the peak value of P_{ii} is increased by more than 5 times. These observations are consistent with the fact that high turbulent intensity appears primarily around the rib height in the V-shaped rib cases (see, Fig. 4). Also from Fig. 6(b), it is observed that owing to the inclined rib geometry, the flow becomes highly disturbed, which tends to distribute TKE to all three directions. As a result, all three production components P_{11}, P_{22} and P_{33} are non-trivial around the rib height. From the partially enlarged figures in Fig. 7, it is clear that negative-valued P_{22} exists near the smooth top wall in both perpendicular and V-shaped ribs. Furthermore, the magnitudes of P_{33} in the V-shaped rib case is much larger than that in the perpendicular rib case. Because of the existence of strong secondary flow, the negative-valued

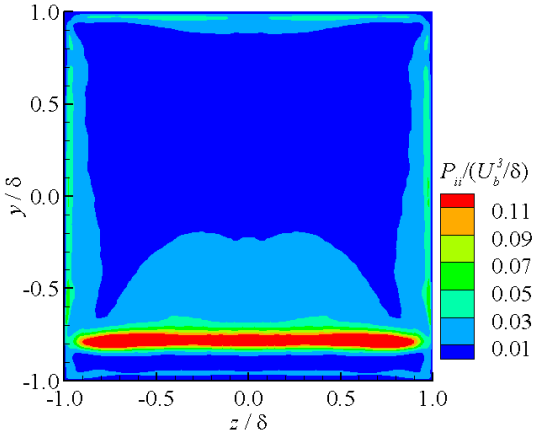

(a) 90° rib case

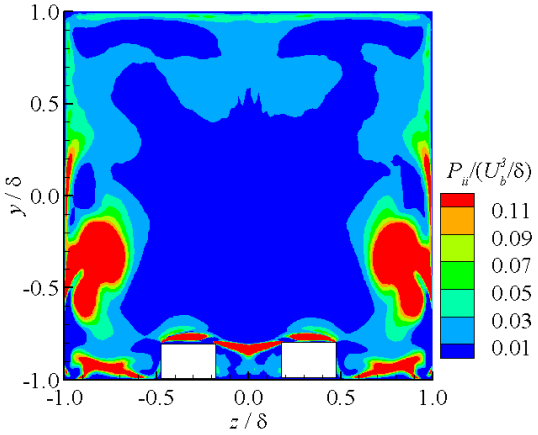

(b) 45° rib case

Figure 6. Contours of the resolved production rate (P_{ii}) of TKE in the y-z plane at $x/\delta = 0.2$ for different rib cases.

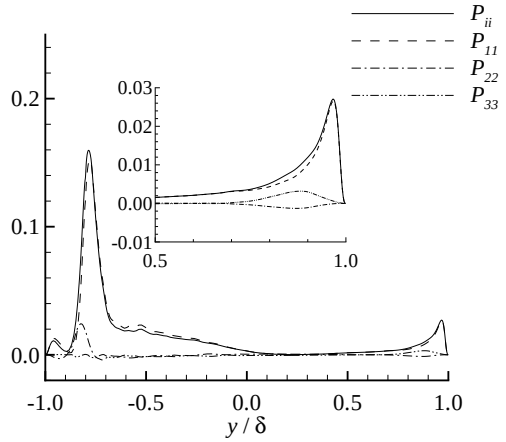

(a) 90° rib case

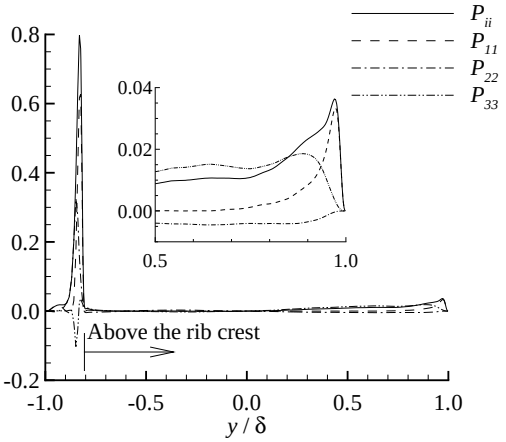

(b) 45° rib case

Figure 7. Vertical profiles of resolved production terms at point $(x/\delta, z/\delta) = (0.2, 0.0)$ for different rib cases.

$\partial \langle \bar{w} \rangle / \partial z$ reaches its maximal magnitude near the top wall, and therefore the level of P_{33} increases considerably due to the contribution from term $-\langle \bar{w}''\bar{w}'' \rangle \partial \langle \bar{w} \rangle / \partial z$. From the above analysis, it is clear that the turbulent flow near the smooth top wall is also significantly altered by the V-shaped ribs on the bottom wall, which demonstrates the 3-D nature of this highly disturbed turbulent flow and intense interaction of the secondary flow with smooth and rib-roughened turbulent boundary layers.

To study the effects of different shaped ribs on turbulent coherent structures, the iso-surface of swirling strength λ_{ci} proposed by Zhou *et al.* (1999) are plotted in Fig. 8 for two different rib cases. In order to effectively demonstrate the elevation of the flow structures, the iso-surfaces are colored using the non-dimensionalized elevation y/δ. As seen from Fig. 8, in comparison with the perpendicular rib case, energetic vortical structures near the central x-y plane for the V-shaped rib case are primarily concentrated in the leeward region of the ribs. This is because the organized large-scale secondary flow appears in the core region of the duct, which impinges onto the bottom wall and downwashes small-scale vortices towards ribs near the midspan. In other words, turbulent vortices are convected towards the leeward region of the ribs by the strong secondary flow in the V-shaped rib cases. This observation is consistent with the experimental results of Fang *et al.* (2015). Furthermore, as clearly shown in Fig. 8(b), in the V-shaped rib case, vortical structures are more populated near the sidewalls, which is consistent with the high levels of turbulent intensity (see, Fig. 5) and TKE production rate (see, Fig. 6) in the same regions.

Conclusion

The highly-disturbed turbulent flow in a square duct with different inclined V-shaped ribs on one wall is studied using LES. The simulation results are validated by comparing the statistics of the first- and second-order moments of the turbulence field against the measured data from the PIV experiments conducted for the same cases by the same authors. The resolved mean velocity, Reynolds shear stresses, turbulent intensities, TKE production rate and coherent flow structures have been analyzed.

The flow features intense interactions of the secondary flows with three smooth and one rib-roughened boundary layers. In the cross-stream directions, secondary flows appear as elongated streamwise vortex pairs in both perpendicular and V-shaped rib cases, and their strength is much stronger in the V-shaped rib cases. As a consequence, a strong downwash near the central region convects the high momentum towards the rib crest. For the V-shaped rib cases, turbulence intensity is suppressed and enhanced near the central region and near two side walls, respectively. The investigation of resolve TKE production term indicates that the induced secondary flow impacts significantly the dis-

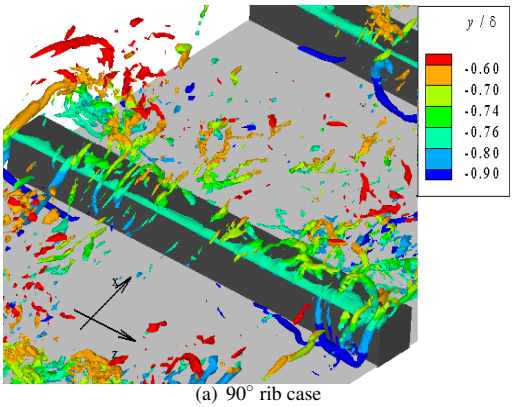

(a) 90° rib case

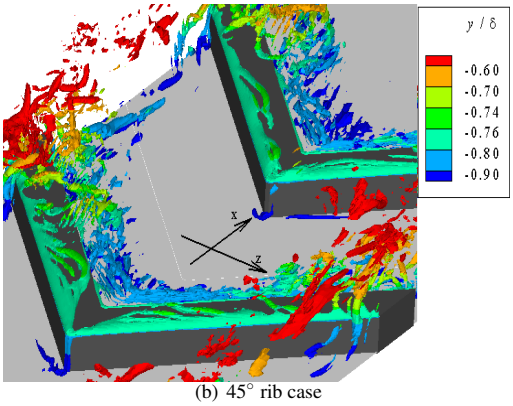

(b) 45° rib case

Figure 8. Iso-surface of λ_{ci} at 5% of the maximal value around different ribs, colored with non-dimensional elevation y/δ.

tribution of TKE in the cross-stream directions. The most energetic turbulent coherent structures in the V-shaped rib cases are mainly concentrated in the leeward of the ribs. This is due to the motion of the large secondary flow, which appears in the central core of the duct and carries small-scale vortices towards the ribbed region.

REFERENCES

Balay, Satish, Abhyankar, Shrirang, Adams, Mark F., Brown, Jed, Brune, Peter, Buschelman, Kris, Eijkhout, Victor, Gropp, William D., Kaushik, Dinesh, Knepley, Matthew G., McInnes, Lois Curfman, Rupp, Karl, Smith, Barry F. & Zhang, Hong 2014*a* PETSc users manual. *Tech. Rep.* ANL-95/11 - Revision 3.5. Argonne National Laboratory.

Balay, Satish, Abhyankar, Shrirang, Adams, Mark F., Brown, Jed, Brune, Peter, Buschelman, Kris, Eijkhout, Victor, Gropp, William D., Kaushik, Dinesh, Knepley, Matthew G., McInnes, Lois Curfman, Rupp, Karl, Smith, Barry F. & Zhang, Hong 2014*b* PETSc Web page. *http://www.mcs.anl.gov/petsc* .

Balay, Satish, Gropp, William D., McInnes, Lois Curfman & Smith, Barry F. 1997 Efficient management of parallelism in object oriented numerical software libraries. In *Modern Software Tools in Scientific Computing* (ed. E. Arge, A. M. Bruaset & H. P. Langtangen), pp. 163–202. Birkhäuser Press.

Bonhoff, B., Parneix, S., Leusch, J., Johnson, B. V., Schabacker, J. & Bölcs, A. 1999 Experimental and numerical study of developed flow and heat transfer in coolant channel with 45 degree ribs. *Int. J. Heat Fluid Flow* **20**, 311–319.

Fang, X., Yang, Z., Wang, B., Tachie, M. F. & Bergstrom, D. J. 2015 Highly-disturbed turbulent flow in a square channel with V-shaped ribs on one wall. *Accepted by Int. J. Heat Fluid Flow* .

Gao, X. & Sundén, B. 2004*a* Effects of inclination angle of ribs on the flow behavior in rectangular ducts. *ASME J. Fuids. Engng.* **126**, 692–699.

Gao, X. & Sundén, B. 2004*b* PIV measurement of the flow field in rectangular ducts with 60° parallel, crossed and V-shaped ribs. *Exper. Thermal Fluid Sci.* **28**, 639–653.

Gavrilakis, S. 1992 Numerical simulation of low-Reynolds-number turbulent flow through a straight square duct. *J. Fluid Mech.* **244**, 101–129.

Kim, J. & Moin, P. 1985 Application of a fractional-step method to incompressible Navier-Stokes equations. *J. Comp. Phys.* **59**, 308–323.

Labbé, O. 2013 Large-eddy-simulation of flow and heat transfer in a ribbed duct. *Comput. Fluids* **76**, 23–32.

Lilly, D. K. 1992 A proposed modification of the Germano subgrid-scale closure method. *Phys. Fluids A* **4**, 633–635.

Murata, A. & Mochizuki, S. 2001 Comparison between laminar and turbulent heat transfer in a stationary square duct with transverse or angled rib turbulators. *Int. J. Heat Mass Trans.* **44**, 1127–1141.

Ooi, A., Iaccario, G., Durbin, P. A. & Behnia, M. 2002 Reynolds averaged simulation of flow and heat transfer in ribbed ducts. *Int. J. Heat Fluid Flow* **23**, 750–757.

Rhie, C. M. & Chow, W. L. 1985 Numerical study of the turbulent flow past an airfoil with trailing edge separation. *AIAA J.* **21**, 1525–1532.

Sewall, E. A., Tafti, D. K., Graham, A. B. & Thole, K. A. 2006 Experimental validation of large eddy simulations of flow and heat transfer in a stationary ribbed duct. *Int. J. Heat Fluid Flow* **27**, 243–258.

Tachie, M. F. & Shah, M. K. 2008 Favorable pressure gradient turbulent flow over straight and inclined ribs on both channel walls. *Phys. Fluids* **20**, 095103.

Taslim, M. E., Kercher, D. M. & Li, T. 1996 Experimental heat transfer and friction in channels roughened with angled, V-shaped, and discrete ribs on two opposite walls. *ASME J. Turbomach.* **118**, 20–28.

Viswanathan, A. K. & Tafti, D. K. 2006 Detached eddy simulation of flow and heat transfer in fully developed rotating internal cooling channel with normal ribs. *Int. J. Heat Fluid Flow* **27**, 351–370.

Zhou, J., Adrian, R. J., Balachandar, S. & Kendall, T. M. 1999 Mechanisms for generating coherent packets of hairpin vortices in channel flow. *J. Fluid Mech.* **387**, 353–396.